Biomedical Optics EXPRESS

Fast blood flow monitoring in deep tissues with real-time software correlators

Detian Wang,[1,2] Ashwin B. Parthasarathy,[1,*] Wesley B. Baker,[1] Kimberly Gannon,[3] Venki Kavuri,[1] Tiffany Ko,[1] Steven Schenkel,[1] Zhe Li,[1,4] Zeren Li,[2] Michael T. Mullen,[3] John A. Detre,[3] and Arjun G. Yodh[1]

[1]*Dept. of Physics and Astronomy, University of Pennsylvania, Philadelphia, PA 19104 USA*
[2]*Interdisciplinary Laboratory of Physics and Biomedicine, Institute of Fluid Physics, China Academy of Engineering Physics, Mianyang 621900, China*
[3]*Div. of Stroke and Neurocritical Care, Hospital of the University of Pennsylvania, Philadelphia, PA 19104 USA*
[4]*State Key Laboratory of Precision Measurement Technology and Instruments, Tianjin University, Tianjin 300072, China*
[*]*ashwinp@sas.upenn.edu*

Abstract: We introduce, validate and demonstrate a new software correlator for high-speed measurement of blood flow in deep tissues based on diffuse correlation spectroscopy (DCS). The software correlator scheme employs standard PC-based data acquisition boards to measure temporal intensity autocorrelation functions continuously at $50-100$ Hz, the fastest blood flow measurements reported with DCS to date. The data streams, obtained *in vivo* for typical source-detector separations of 2.5 cm, easily resolve pulsatile heart-beat fluctuations in blood flow which were previously considered to be noise. We employ the device to separate tissue blood flow from tissue absorption/scattering dynamics and thereby show that the origin of the pulsatile DCS signal is primarily flow, and we monitor cerebral autoregulation dynamics in healthy volunteers more accurately than with traditional instrumentation as a result of increased data acquisition rates. Finally, we characterize measurement signal-to-noise ratio and identify count rate and averaging parameters needed for optimal performance.

OCIS codes: (030.0030) Speckle; (030.5290) Photon Statistics; (030.5260) Photon Counting; (170.3880) Medical and Biological Imaging; (170.1610) Clinical Applications; (110.4153) Motion estimation and optical flow; (170.2655) Functional monitoring and imaging; (170.1470) Blood or tissue constituent monitoring; (290.4210) Multiple scattering; (170.5270) Photon density waves; (170.6510) Spectroscopy, tissue diagnostics; (170.6480) Spectroscopy, speckle.

References and links

1. D. A. Boas, L. E. Campbell, and A. G. Yodh, "Scattering and imaging with diffusing temporal field correlations," Phy. Rev. Lett. **75**, 1855–1858 (1995).
2. D. A. Boas and A. G. Yodh, "Spatially varying dynamical properties of turbid media probed with diffusing temporal light correlation," J. Opt. Soc. Am. A **14**, 192–215 (1997).
3. T. Durduran and A. G. Yodh, "Diffuse correlation spectroscopy for non-invasive, micro-vascular cerebral blood flow measurement," NeuroImage **85 Pt 1**, 51–63 (2014).
4. G. Yu, "Diffuse Correlation Spectroscopy (DCS): A Diagnostic Tool for Assessing Tissue Blood Flow in Vascular-Related Diseases and Therapies," Curr. Med. Im. Rev. **8**, 194–210 (2012).

#255500 Received 14 Dec 2015; revised 20 Jan 2016; accepted 21 Jan 2016; published 3 Feb 2016

5. E. M. Buckley, A. B. Parthasarathy, P. E. Grant, A. G. Yodh, and M. A. Franceschini, "Diffuse correlation spectroscopy for measurement of cerebral blood flow: future prospects," Neurophotonics **1**, 011009 (2014).
6. C. G. Favilla, R. C. Mesquita, M. Mullen, T. Durduran, X. Lu, M. N. Kim, D. L. Minkoff, S. E. Kasner, J. H. Greenberg, A. G. Yodh, and J. A. Detre, "Optical bedside monitoring of cerebral blood flow in acute ischemic stroke patients during head-of-bed manipulation," Stroke **45**, 1269–1274 (2014).
7. R. C. Mesquita, T. Durduran, G. Yu, E. M. Buckley, M. N. Kim, C. Zhou, R. Choe, U. Sunar, and A. G. Yodh, "Direct measurement of tissue blood flow and metabolism with diffuse optics," Philos. Trans. Ser. A: Math. Phys. Eng. Sci. **369**, 4390–4406 (2011).
8. T. Durduran, R. Choe, W. B. Baker, and A. G. Yodh, "Diffuse optics for tissue monitoring and tomography," Rep. Prog. Phy. **73**, 076701 (2010).
9. E. M. Buckley, D. Hance, T. Pawlowski, J. M. Lynch, F. B. Wilson, R. C. Mesquita, T. Durduran, L. K. Diaz, M. E. Putt, D. J. Licht, M. A. Fogel, and A. G. Yodh, "Validation of diffuse correlation spectroscopic measurement of cerebral blood flow using phase-encoded velocity mapping magnetic resonance imaging," J. Biomed. Opt. **17**, 037007 (2012).
10. E. M. Buckley, N. M. Cook, T. Durduran, M. N. Kim, C. Zhou, R. Choe, G. Yu, S. Schultz, C. M. Sehgal, D. J. Licht, P. H. Arger, M. E. Putt, H. H. Hurt, and A. G. Yodh, "Cerebral hemodynamics in preterm infants during positional intervention measured with diffuse correlation spectroscopy and transcranial Doppler ultrasound." Opt. Express **17**, 12571–12581 (2009).
11. V. Jain, E. M. Buckley, D. J. Licht, J. M. Lynch, P. J. Schwab, M. Y. Naim, N. A. Lavin, S. C. Nicolson, L. M. Montenegro, A. G. Yodh, and F. W. Wehrli, "Cerebral oxygen metabolism in neonates with congenital heart disease quantified by MRI and optics," J. Cereb. Blood Flow Metab. **34**, 380–388 (2013).
12. T. Durduran, C. Zhou, E. M. Buckley, M. N. Kim, G. Yu, R. Choe, J. W. Gaynor, T. L. Spray, S. M. Durning, S. E. Mason, L. M. Montenegro, S. C. Nicolson, R. A. Zimmerman, M. E. Putt, J. Wang, J. H. Greenberg, J. A. Detre, A. G. Yodh, and D. J. Licht, "Optical measurement of cerebral hemodynamics and oxygen metabolism in neonates with congenital heart defects." J. Biomed. Opt. **15**, 037004 (2010).
13. T. Durduran, C. Zhou, B. L. Edlow, G. Yu, R. Choe, M. N. Kim, B. L. Cucchiara, M. E. Putt, Q. Shah, S. E. Kasner, J. H. Greenberg, A. G. Yodh, and J. A. Detre, "Transcranial optical monitoring of cerebrovascular hemodynamics in acute stroke patients." Opt. Express **17**, 3884–3902 (2009).
14. M. N. Kim, B. L. Edlow, T. Durduran, S. Frangos, R. C. Mesquita, J. M. Levine, J. H. Greenberg, A. G. Yodh, and J. A. Detre, "Continuous optical monitoring of cerebral hemodynamics during head-of-bed manipulation in brain-injured adults," Neurocrit. Care **20**, 443–445 (2014).
15. M. N. Kim, T. Durduran, S. Frangos, B. L. Edlow, E. M. Buckley, H. E. Moss, C. Zhou, G. Yu, R. Choe, E. Maloney-Wilensky, R. L. Wolf, M. S. Grady, J. H. Greenberg, J. M. Levine, A. G. Yodh, J. A. Detre, and W. A. Kofke, "Noninvasive measurement of cerebral blood flow and blood oxygenation using near-infrared and diffuse correlation spectroscopies in critically brain-injured adults," Neurocrit. Care **12**, 173–180 (2010).
16. R. C. Mesquita, M. Putt, M. Chandra, G. Yu, X. Xing, S. W. Han, G. Lech, Y. Shang, T. Durduran, C. Zhou, A. G. Yodh, and E. R. Mohler, "Diffuse optical characterization of an exercising patient group with peripheral artery disease," J. Biomed. Opt. **18**, 057007 (2013).
17. Y. Shang, K. Gurley, and G. Yu, "Diffuse Correlation Spectroscopy (DCS) for Assessment of Tissue Blood Flow in Skeletal Muscle: Recent Progress," Anat. Physiol. **03**, 128 (2013).
18. R. Choe, M. E. Putt, P. M. Carlile, T. Durduran, J. M. Giammarco, D. R. Busch, K. W. Jung, B. J. Czerniecki, J. C. Tchou, M. D. Feldman, C. Mies, M. A. Rosen, M. D. Schnall, A. DeMichele, and A. G. Yodh, "Optically Measured Microvascular Blood Flow Contrast of Malignant Breast Tumors," PLoS ONE **9**, e99683 (2014).
19. T. Durduran, R. Choe, G. Yu, C. Zhou, J. C. Tchou, B. J. Czerniecki, and A. G. Yodh, "Diffuse optical measurement of blood flow in breast tumors," Opt. Lett. **30**, 2915 (2005).
20. U. Sunar, H. Quon, T. Durduran, J. Zhang, J. Du, C. Zhou, G. Yu, R. Choe, A. Kilger, R. Lustig, L. Loevner, S. Nioka, B. Chance, and A. G. Yodh, "Noninvasive diffuse optical measurement of blood flow and blood oxygenation for monitoring radiation therapy in patients with head and neck tumors: a pilot study," J. Biomed. Opt. **11**, 064021 (2006).
21. G. Yu, "Near-infrared diffuse correlation spectroscopy in cancer diagnosis and therapy monitoring," J. Biomed. Opt. **17**, 010901 (2012).
22. W. B. Baker, A. B. Parthasarathy, T. S. Ko, D. R. Busch, K. Abramson, S.-Y. Tzeng, R. C. Mesquita, T. Durduran, J. H. Greenberg, D. K. Kung, and A. G. Yodh, "Pressure modulation algorithm to separate cerebral hemodynamic signals from extracerebral artifacts," Neurophotonics **2**, 035004 (2015).
23. T. Durduran, G. Yu, M. G. Burnett, J. A. Detre, J. H. Greenberg, J. Wang, C. Zhou, and A. G. Yodh, "Diffuse optical measurement of blood flow, blood oxygenation, and metabolism in a human brain during sensorimotor cortex activation." Opt. Lett. **29**, 1766–1768 (2004).
24. F. Jaillon, J. Li, G. Dietsche, T. Elbert, and T. Gisler, "Activity of the human visual cortex measured noninvasively by diffusing-wave spectroscopy." Opt. Express **15**, 6643–6650 (2007).
25. J. Li, M. Ninck, L. Koban, T. Elbert, J. Kissler, and T. Gisler, "Transient functional blood flow change in the human brain measured noninvasively by diffusing-wave spectroscopy," Opt. Lett. **33**, 2233–2235 (2008).
26. N. Roche-Labarbe, A. Fenoglio, H. Radhakrishnan, M. Kocienski-Filip, S. A. Carp, J. Dubb, D. A. Boas, P. E.

#255500 Received 14 Dec 2015; revised 20 Jan 2016; accepted 21 Jan 2016; published 3 Feb 2016

Grant, and M. A. Franceschini, "Somatosensory evoked changes in cerebral oxygen consumption measured non-invasively in premature neonates," NeuroImage **85**, 279–286 (2014).
27. T. Binzoni and F. Martelli, "Assessing the reliability of diffuse correlation spectroscopy models on noise-free analytical Monte Carlo data," Appl. Opt. **54**, 5320–5326 (2015).
28. W. B. Baker, A. B. Parthasarathy, D. R. Busch, R. C. Mesquita, J. H. Greenberg, and A. G. Yodh, "Modified Beer-Lambert law for blood flow," Biomed. Opt. Express **5**, 4053–4075 (2014).
29. R. Sriram Chandran, G. Devaraj, R. Kanhirodan, D. Roy, and R. M. Vasu, "Detection and estimation of liquid flow through a pipe in a tissue-like object with ultrasound-assisted diffuse correlation spectroscopy," J. Opt. Soc. Am. A **32**, 1888–1897 (2015).
30. A. Tsalach, Z. Schiffer, E. Ratner, I. Breskin, R. Zeitak, R. Shechter, and M. Balberg, "Depth selective acousto-optic flow measurement," Biomed. Opt. Express **6**, 4871–4886 (2015).
31. L. Gagnon, M. Desjardins, J. Jehanne-Lacasse, L. Bherer, and F. Lesage, "Investigation of diffuse correlation spectroscopy in multi-layered media including the human head." Opt. Express **16**, 15514–15530 (2008).
32. Y. Shang and G. Yu, "A Nth-order linear algorithm for extracting diffuse correlation spectroscopy blood flow indices in heterogeneous tissues," Appl. Phy. Lett. **105**, 133702 (2014).
33. K. Gurley, Y. Shang, and G. Yu, "Noninvasive optical quantification of absolute blood flow, blood oxygenation, and oxygen consumption rate in exercising skeletal muscle," J. Biomed. Opt. **17**, 0750101 (2012).
34. Z. Li, W. B. Baker, A. B. Parthasarathy, T. S. Ko, D. Wang, S. S. Schenkel, T. Durduran, G. Li, and A. G. Yodh, "Calibration of diffuse correlation spectroscopy blood flow index with venous-occlusion diffuse optical spectroscopy in skeletal muscle," J. Biomed. Opt. **20** 125005 (2015).
35. S. A. Carp, G. P. Dai, D. A. Boas, M. A. Franceschini, and Y. R. Kim, "Validation of diffuse correlation spectroscopy measurements of rodent cerebral blood flow with simultaneous arterial spin labeling MRI; towards MRI-optical continuous cerebral metabolic monitoring," Biomed. Opt. Express **1**, 553 (2010).
36. M. Diop, K. Verdecchia, T.-Y. Lee, and K. St Lawrence, "Calibration of diffuse correlation spectroscopy with a time-resolved near-infrared technique to yield absolute cerebral blood flow measurements," Biomed. Opt. Express **2**, 2068–2081 (2011).
37. R. C. Mesquita, O. K. Faseyitan, P. E. Turkeltaub, E. M. Buckley, A. Thomas, M. N. Kim, T. Durduran, J. H. Greenberg, J. A. Detre, A. G. Yodh, and R. H. Hamilton, "Blood flow and oxygenation changes due to low-frequency repetitive transcranial magnetic stimulation of the cerebral cortex," J. Biomed. Opt. **18**, 067006 (2013).
38. E. M. Buckley, J. M. Lynch, D. A. Goff, P. J. Schwab, W. B. Baker, T. Durduran, D. R. Busch, S. C. Nicolson, L. M. Montenegro, M. Y. Naim, R. Xiao, T. L. Spray, A. G. Yodh, J. W. Gaynor, and D. J. Licht, "Early postoperative changes in cerebral oxygen metabolism following neonatal cardiac surgery: Effects of surgical duration," J. Thorac. Cardiovasc. Surg. **145**, 196–205 (2013).
39. J. M. Lynch, E. M. Buckley, P. J. Schwab, A. L. McCarthy, M. E. Winters, D. R. Busch, R. Xiao, D. A. Goff, S. C. Nicolson, L. M. Montenegro, S. Fuller, J. W. Gaynor, T. L. Spray, A. G. Yodh, M. Y. Naim, and D. J. Licht, "Time to surgery and preoperative cerebral hemodynamics predict postoperative white matter injury in neonates with hypoplastic left heart syndrome," J. Thorac. Cardiovasc. Surg. **148**, 2181–2188 (2014).
40. F. P. Tiecks, A. M. Lam, R. Aaslid, and D. W. Newell, "Comparison of static and dynamic cerebral autoregulation measurements." Stroke **26**, 1014–1019 (1995).
41. R. Aaslid, K.-F. Lindegaard, W. Sorteberg, and H. Nornes, "Cerebral autoregulation dynamics in humans," Stroke **20**, 45–52 (1989).
42. Y. Shang, T. B. Symons, T. Durduran, A. G. Yodh, and G. Yu, "Effects of muscle fiber motion on diffuse correlation spectroscopy blood flow measurements during exercise," Biomed. Opt. Express **1**, 500–511 (2010).
43. D. Magatti and F. Ferri, "Fast Multi-Tau Real-Time Software Correlator for Dynamic Light Scattering," Appl. Opt. **40**, 4011–4021 (2001).
44. D. Magatti and F. Ferri, "25 ns software correlator for photon and fluorescence correlation spectroscopy," Rev. Sci. Instr. **74**, 1135–1144 (2003).
45. K. Schatzel, "Correlation techniques in dynamic light scattering," Appl. Phys. B **42**, 193–213 (1987).
46. K. Schatzel, "Noise on photon correlation data. I. Autocorrelation functions," Quant. Opt. **2**, 287–305 (1990).
47. K. Schatzel, M. Drewel, and S. Stimac, "Photon Correlation Measurements at Large Lag Times: Improving Statistical Accuracy," J. Mod. Opt. **35**, 711–718 (2007).
48. J. Selb, D. A. Boas, S.-T. Chan, K. C. Evans, E. M. Buckley, and S. A. Carp, "Sensitivity of near-infrared spectroscopy and diffuse correlation spectroscopy to brain hemodynamics: simulations and experimental findings during hypercapnia," Neurophotonics **1**, 015005 (2014).
49. A. Middleton and D. Fisher, "Discrete scatterers and autocorrelations of multiply scattered light." Phys. Rev. B **43**, 5934–5938 (1991).
50. G. Dietsche, M. Ninck, C. Ortolf, J. Li, F. Jaillon, and T. Gisler, "Fiber-based multispeckle detection for time-resolved diffusing-wave spectroscopy: characterization and application to blood flow detection in deep tissue." Appl. Opt. **46**, 8506–8514 (2007).
51. J. Li, F. Jaillon, G. Dietsche, G. Maret, and T. Gisler, "Pulsation-resolved deep tissue dynamics measured with diffusing-wave spectroscopy," Opt. Express **14**, 7841 (2006).
52. J. Dong, R. Bi, J. H. Ho, P. S. P. Thong, K.-C. Soo, and K. Lee, "Diffuse correlation spectroscopy with a fast

#255500 Received 14 Dec 2015; revised 20 Jan 2016; accepted 21 Jan 2016; published 3 Feb 2016

Fourier transform-based software autocorrelator," J. Biomed. Opt. **17**, 0970041 (2012).
53. M. Tivnan, R. Gurjar, D. Wolf, and K. Vishwanath, "High Frequency Sampling of TTL Pulses on a Raspberry Pi for Diffuse Correlation Spectroscopy Applications," Sensors **15**, 19709–19722 (2015).
54. National Instruments white paper, "Application Design Patterns: Producer/Consumer," (National Instruments, 2012) http://www.ni.com/white-paper/3023/en/.
55. S. Strandgaard and O. B. Paulson, "Cerebral autoregulation," Stroke **15**, 413–416 (1984).
56. M. Jaeger, M. Soehle, M. U. Schuhmann, and J. Meixensberger, "Clinical Significance of Impaired Cerebrovascular Autoregulation After Severe Aneurysmal Subarachnoid Hemorrhage," Stroke **43**, 2097–2101 (2012).
57. S. L. Dawson, R. B. Panerai, and J. F. Potter, "Serial Changes in Static and Dynamic Cerebral Autoregulation after Acute Ischaemic Stroke," Cerebrovasc. Diseases **16**, 69–75 (2003).
58. M. Jaeger, M. U. Schuhmann, M. Soehle, C. Nagel, and J. Meixensberger, "Continuous Monitoring of Cerebrovascular Autoregulation After Subarachnoid Hemorrhage by Brain Tissue Oxygen Pressure Reactivity and Its Relation to Delayed Cerebral Infarction," Stroke **38**, 981–986 (2007).
59. R. Cheng, Y. Shang, D. Hayes, Jr, S. P. Saha, and G. Yu, "Noninvasive optical evaluation of spontaneous low frequency oscillations in cerebral hemodynamics," NeuroImage **62**, 1445–1454 (2012).
60. M. Reinhard, E. Wehrle-Wieland, D. Grabiak, M. Roth, B. Guschlbauer, J. Timmer, C. Weiller, and A. Hetzel, "Oscillatory cerebral hemodynamics—the macro- vs. microvascular level," J. Neurolog. Sciences **250**, 103–109 (2006).
61. S. Fantini, "Dynamic model for the tissue concentration and oxygen saturation of hemoglobin in relation to blood volume, flow velocity, and oxygen consumption: Implications for functional neuroimaging and coherent hemodynamics spectroscopy (CHS)." NeuroImage **85 Pt 1**, 202–221 (2014).
62. C. Zhou, G. Yu, D. Furuya, J. H. Greenberg, A. G. Yodh, and T. Durduran, "Diffuse optical correlation tomography of cerebral blood flow during cortical spreading depression in rat brain." Opt. Express **14**, 1125–1144 (2006).
63. R. J. Cooper, J. Selb, L. Gagnon, D. Phillip, H. W. Schytz, H. K. Iversen, M. Ashina, and D. A. Boas, "A Systematic Comparison of Motion Artifact Correction Techniques for Functional Near-Infrared Spectroscopy," Fron. Neurosci. **6**, 147 (2012).
64. T. J. Huppert, S. G. Diamond, M. A. Franceschini, and D. A. Boas, "HomER: a review of time-series analysis methods for near-infrared spectroscopy of the brain," Appl. Opt. **48**, D280–D298 (2009).
65. J. M. Kainerstorfer, A. Sassaroli, and S. Fantini, "Coherent hemodynamics spectroscopy in a single step," Biomed. Opt. Express **5**, 3403 (2014).
66. P. A. Lemieux and D. J. Durian, "Investigating non-Gaussian scattering processes by using nth-order intensity correlation functions," J. Opt. Soc. Am. A **16**, 1651 (1999).

1. Introduction

Blood flow is a clinical biomarker for tissue health because of its importance for oxygen delivery and clearance of metabolic byproducts, and Diffuse Correlation Spectroscopy (DCS) [1, 2] is emerging as the non-invasive optical method of choice to measure blood flow in tissues located $1-3$ cms below the surface [3–7]. Nevertheless, despite attributes such as suitability for bedside monitoring and sensitivity to tissue microvasculature [2, 3, 5, 8], as well as numerous clinical applications [6, 7, 9–26], the full potential of DCS as a clinical blood flow monitor will only be realized when several technical limitations [5, 27] are ameliorated. Methods to remove the confounding influence of flow in superficial tissues, for example, are under development but need more validation [22, 28–32]. Similarly, methods for absolute calibration of blood flow have been developed and tested with some success [33–36], but more work is needed.

A third limitation and opportunity for improvement concerns data throughput, *e.g.*, measurement time resolution and acquisition rate. Most DCS measurements of blood flow are slow, with measurement sampling rates ranging from 0.3 to 1 Hz. Thus DCS has only been used to measure flow variation over slow time scales, *i.e.*, measurements every minute/hour [10, 13, 37, 38], or measurements every day [39]. Indeed, fast cerebral blood flow (CBF) measurements ($25-50$ Hz) can enable new applications for DCS, such as monitoring cerebrovascular autoregulation dynamics [40,41] wherein beat-to-beat variability of both blood pressure and blood flow are used to characterize autoregulation. High temporal resolution measurements will also improve identification of motion artifacts and thereby create potential for measuring tissue blood flow during exercise [42]. Finally, fast sampling increases measurement throughput and will

#255500 Received 14 Dec 2015; revised 20 Jan 2016; accepted 21 Jan 2016; published 3 Feb 2016

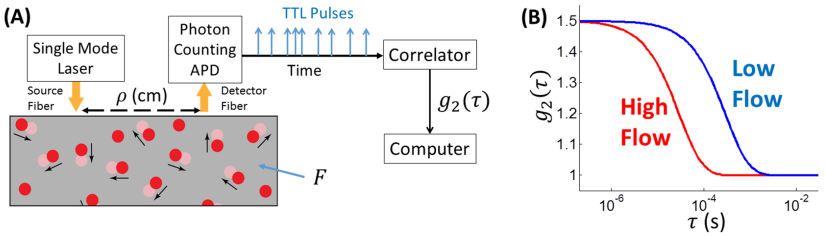

Fig. 1. (A) Schematic of DCS instrumentation in the semi-infinite geometry. Highly coherent single mode laser light is used to illuminate the sample via optical fibers. Red blood cell motion (*e.g.*, red disks to light red disks in time τ; blood flow F) causes fluctuations in the intensity of backscattered light that is collected a distance ρ away from the source, and is directed to single photon counting avalanche photo diodes (APDs). A correlator counts the arrival of digital TTL pulses generated by the APDs to compute the DCS autocorrelation functions, (B) Sample intensity autocorrelation functions ($g_2(\tau)$) highlighting different flow rates.

enable high *spatial* resolution imaging with fewer detectors. For example, photons collected from many $(32-48)$ detector positions can be routed to a few $(4-8)$ photon detectors via an optical switch. In these cases, besides the obvious cost advantages, fast sampling can reduce the imaging frame rate to seconds or less (rather than minutes), thus enabling dynamic *imaging*.

In this contribution we report on the development of a novel software correlator optimized for continuous, high-speed monitoring of deep tissue blood flow based on diffuse correlation spectroscopy (DCS). This device uses the 'shift-and-add' method [43, 44] to directly compute the correlation function at a few (40), highly relevant delay times ($1\mu s \leq \tau \leq 250\mu s$). Leveraging this data compression and other technological improvements, we demonstrate sustained blood flow measurement speeds up to 100 Hz with 8 simultaneous detection channels (and up to 1 kHz with 2 detection channels). To our knowledge, these experiments represent the fastest measurements of blood flow with DCS. The fast data streams easily resolve pulsatile heart-beat fluctuations in blood flow which were previously treated as noise, and they enable us to monitor cerebral autoregulation dynamics more accurately than with traditional instrumentation.

The remainder of this paper is organized as follows. We first provide context for our work with respect to traditional flow measurement devices and other software correlators. Next, we describe the software correlator instrumentation and validate its measurements *in vivo* with a hardware correlator. We then highlight the utility of the fast correlator for two *in vivo* applications. First, we measure the pulsatile arterial blood flow with DCS; in the process we separate the tissue blood flow components in the dynamical signal from tissue absorption/scattering components. Second, we measure cerebral autoregulation dynamics in healthy adults. Finally, we characterize the effect of averaging and photon count rate on measurement signal-to-noise ratio.

2. Correlation methods: background and new features

The fast data throughput improvements are best appreciated by comparison to traditional methods utilized for DCS measurements [2–5]. Briefly, DCS employs coherent near-infrared light to characterize moving particles (red blood cells) in tissue via temporal light intensity fluctuations. Figure 1 shows a schematic of the typical DCS instrument. Laser light illuminates the tissue. An optical fiber, placed on the surface $\sim 2-3$ cms away from the source, collects light that has diffused through the tissue and directs it to a photon counting detector that generates an electrical Transistor-Transistor Logic (TTL) digital pulse for every detected photon. A cor-

#255500 Received 14 Dec 2015; revised 20 Jan 2016; accepted 21 Jan 2016; published 3 Feb 2016

relator records the arrival of TTL pulses and uses the distribution of arrival times to quantify the temporal fluctuations of detected light intensity. Formally, the correlator calculates the normalized intensity autocorrelation function ($g_2(\tau)$) from measurements of the photon intensity, $g_2(\tau) \equiv \langle I(t)I(t+\tau)\rangle / \langle I(t)\rangle^2$, where, $I(t)$ is the detected intensity at time t, τ is the correlation delay time, and $\langle\rangle$ represent time-averages. Blood flow is estimated by fitting the measured intensity autocorrelation function to mathematical models appropriate to the measurement geometry.

The rapid adoption of DCS for clinical flow monitoring was aided by the availability of user-friendly and convenient hardware correlators (*e.g.*, Correlator.com, Bridgewater, New Jersey; ALB, Hessen, Germany), but this convenience also limited measurement speed. Traditionally, correlators employ embedded programming and a multi-tau algorithm [45–47] to compute the autocorrelation functions over a large range of delay times (from $\sim 1\mu$s up to as much as $1 \sim 2$s); this design follows from early dynamic light scattering (DLS) and diffusing wave spectroscopy (DWS) experiments in mostly non-biological samples [43–47]. DCS intensity autocorrelation functions from deep tissue blood flow, however, typically decay at a much faster rates than in DLS experiments [3, 8], and exhibit other slow dynamics at heart rate frequencies (and even faster). Deep tissue $g_2(\tau)$ most often decays to 1 at delay times of $\tau \sim 250\mu$s or less (see Fig. 1(B)). Thus, correlation data at delay times greater than $\sim 250\mu$s does not offer significant information about tissue dynamics. Furthermore, the autocorrelation function at short delay times is more sensitive to photons that travel deep into tissue, *i.e.*, the photons we care about [28,48,49], and blood flow *changes* can be estimated from DCS autocorrelation functions at a *single* delay-time [28]. Thus, many reasons exist for data-set reduction/compression, and by reducing the number of delay-times in the correlation function calculation, our data acquisition can be made more efficient and faster.

Unfortunately, reconfiguration of commercial correlators that are pre-optimized for general applications is nontrivial; reconfiguration involves reprogramming of the embedded correlator circuits with specialized equipment. Nevertheless, some precedence for fast blood flow measurements exists with hardware correlators, albeit with limitations. Of note is the work of Dietsche et. al. [50] who used a hardware correlator in the so-called 'burst' mode to measure blood flow at ~ 40 Hz; the measurement was fast enough to detect pulsatile blood flow in the human arm and forehead at source-detector separations of $1.4 \sim 1.9$ cm. However, the measurements required either averaging of correlation functions from many $(16-32)$ detectors at a single point in space [50], or the use of a dual-mode correlator and 2 detectors gated at the pulse rate [51]. Importantly, burst mode correlators store rapidly acquired normalized intensity autocorrelation functions on an internal memory buffer which only has space for approximately 1000 correlation functions [50]. Thus, they are designed for sustained high speed acquisition over short time intervals (~ 20 s [50]) and cannot be easily used for continuous long-term monitoring. Moreover, data transfer interfaces and program drivers employed to transfer the correlation functions to a computer are not optimized for speed. Therefore, even though actual computation of correlation functions on the hardware correlator can be fast, programming overhead issues result in blood flow measurements at speeds only as fast as $1 \sim 2$ Hz (for standard correlators).

Computation of correlation functions in software rather than hardware, *i.e.*, the software correlator, offers a flexible alternative approach that greatly facilitates optimization of the correlation measurement for deep tissue blood flow with DCS. The software correlators also utilize digital counters to record TTL pulses from the photon counting detectors [43, 44, 52, 53]. Instead of computing the correlation function with embedded programming, however, high-level programs (*e.g.* LabVIEW, C++) control the counter readout and estimate the correlation function in the computer's random access memory (RAM). Proof-of-principle measurements with

#255500 Received 14 Dec 2015; revised 20 Jan 2016; accepted 21 Jan 2016; published 3 Feb 2016

diffuse correlation spectroscopy via the Wiener-Khinchin theorem, *i.e.*, the convolution of the measured temporal intensity and its time-reversed duplicate have been made with software correlators [52, 53]. These studies did not optimize the correlation function computations for measurement speed, and this approach requires a large buffer to store the stream of detected photon pulses each second, *e.g.*, data sampling rates smaller than 2 μs would fill a typical computer's buffer in less than a second [52]. Thus, continuous blood flow monitoring over long time intervals with this approach is not practical (as was the case with the burst mode correlator).

Our approach utilizes the 'shift-and-add' method [43, 44], to directly compute the correlation function; this scheme is technically similar to that of hardware correlators. Importantly, we leverage several technical advances. First, we employ a data reduction/compression strategy, *i.e.*, the correlation function is measured at only a few biologically relevant delay times (40 delays; $1\mu\text{s} \leq \tau \leq 250\mu\text{s}$). Second, we employ an improved instrument design, *i.e.*, the photon counters are directly connected to the computer's PCI-bus, eliminating the need for USB-software drivers. Finally, our software design substantially reduces data transfer overheads. The present contribution thus describes an approach to simplify and optimize computation of correlation functions for deep tissue blood flow monitoring with DCS. Importantly, this flexible solution can be implemented/adapted to any existing DCS system with modest instrumentation upgrades. The design of this improved software correlator is described in detail below.

3. Real-time software correlator: design and instrumentation

Our real-time software correlator is implemented on a personal computer (Dell Inspiron, Intel core i5 − 4200M, Dual Core, 8GB RAM) using a dedicated 8 channel PCIe/PXIe6612 counter/timer data acquisition board (National Instruments, Austin, TX) and a custom software program (LabVIEW, National Instruments, Austin, TX). As shown schematically in Fig. 1(A), a stream of digital TTL pulses generated by the photon counting APD is directed to an edge-detecting photon counter on the PCIe6612 data acquisition board. The operation is diagrammed in Fig. 2(B). Briefly, the counter's operations are synchronized by an internal timebase (set to 80 MHz by default). At every clock-tick of the timebase, the counter seeks a TTL signal at its input terminal, and if the TTL pulse is present, then the counter increments and updates its internal count by 1. The photon counts are then transferred to an internal buffer at a user-defined sampling clock frequency ($f_s = 1/\Delta t$). By generating the sampling clock based on the data acquisition board's built-in frequency generator, we ensure that counter timing/sampling is unaffected by computer processing operations. The counter buffer ($N(i)$) is allowed to accumulate counts over a user-defined integration time (t_{int}), and then $n_{int} = f_s \times t_{int}$ points of the buffer are transferred to the computer for calculation of the correlation function. Thus, $N(i)$ represents the number of counts that have been accumulated through the i^{th} sample interval in the counter buffer.

Since the counter continuously accumulates photon counts, the quasi-instantaneous photon count during the small time interval at index i (*i.e.*, $n(i)$) is calculated as $n(i) = N(i+1) - N(i)$. The normalized intensity autocorrelation at delay time $\tau = \Delta n / f_s$ is then estimated from:

$$g_2(\Delta n = \tau f_s) = \frac{\langle n(i) n(i+\Delta n) \rangle}{\langle n(i) \rangle \langle n(i) \rangle} \tag{1}$$

where, $\langle\rangle$ represent time averages over $n_{avg} = n_{int} - \Delta n$ points. Notice, the smallest delay time in the computation of the autocorrelation function is $(1/f_s)$ s, and the correlation function detection frame rate is $(1/t_{int})$ Hz. In our implementation of the software correlator, $f_s = 1$ MHz, while t_{int} can vary from 1 ms to 1 s. For a typical *in vivo* experiment, $t_{int} \sim 40$ ms. The custom software correlator computes the normalized autocorrelation function using Eq. (1) over 40 delay times ($1\ \mu$s to $\sim 125\ \mu$s) from 8 channels simultaneously. Real-time computation of the

#255500 Received 14 Dec 2015; revised 20 Jan 2016; accepted 21 Jan 2016; published 3 Feb 2016

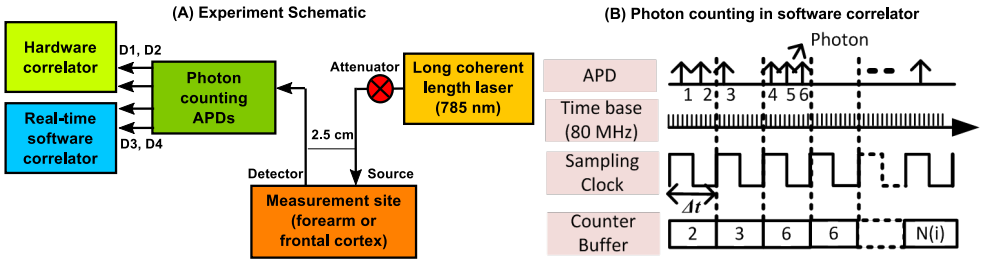

Fig. 2. (A) Block diagram of experiment setup for *in vivo* studies. Long coherence length near-infrared light illuminates the tissue. Diffuse light is collected via a 4×1 bundle of single mode fibers 2.5 cms away on the surface for detection. Two detection channels are directed to a commercial hardware and two more to the custom software correlator. (B) Schematic operation of software correlator. TTL pulses generated by the APDs are counted using an 80 MHz internal counter time base. Accumulated photon counts are transferred to a counter buffer ($N(i)$) at a user defined sampling frequency ($f_s = 1/\Delta t$). $N(i)$ denotes the i^{th} sample in the counter buffer, *i.e.*, the number of counts that have been accumulated through the i^{th} sample interval.

correlation function is ensured via buffered producer-consumer loops [54].

The high acquisition rate is in part due to more time-efficient software architecture. Moreover, computing the autocorrelation function over a relatively small range of delay times greatly simplifies the software operations; a smaller range of delay times permits use of the simpler single-tau correlator design wherein photons do not have to be temporally binned as in multi-tau correlators [44]. More significantly, the smaller delay-time range permits smaller integration times. For example, from Eq. (1) one can infer that the minimum number of points, n_{int}, required to estimate the correlation function is $\Delta n + 1$. Computation of the correlation function at large delay times, *i.e.*, larger Δn, will necessitate larger n_{int} (and consequently larger integration times, t_{int}) to ensure that $n_{Avg} \gg 1$. As we have previously described, DCS intensity correlation functions decay to their minimum value at delay times < 200 μs, and measurements beyond these time scales are superfluous.

We close this section with a note about timing and sampling considerations. In general, the temporal response time of the APD will limit the maximum number of photons that can be *detected* in one second, while the counter timebase (80 MHz) places a limit on the frequency of TTL pulses (*i.e.*, photons), that can be *counted*. The most popular/common single photon counting APD used for DCS (SPCM-AQ4C, Excelitas, Quebec, Canada) has a temporal response time of 25 ns, and a response 'dead time' of 50 ns. Thus the maximum photon count rate that the APD can *detect* is ~ 13.3 MHz, which is sufficiently small compared to the default counter timebase of 80 MHz. Nevertheless, the relative differences between the APD response time and the counter timebase are important design considerations for the software correlator.

4. Experiments and results

All blood flow measurements were carried out using a custom DCS instrument (Fig. 2(A)) [22, 28]. Briefly, a continuous wave, long coherence length (> 5 m) fiber coupled laser (785 nm, 80 mW, DL785-100-3O, CrystaLaser Inc., Reno, NV) was used to illuminate the sample via a multimode fiber (200 μm diameter, OZ Optics, Ottawa, Canada). Remitted light that travelled through the sample is detected by a bundle of single mode fibers (5 μm diameter, OZ Optics, Ottawa, Canada) located 2.5 cms away from the source. Each detector fiber directs light to a single photon counting APD (SPCM-AQ4C, Excelitas, Quebec, Canada). For compar-

#255500 Received 14 Dec 2015; revised 20 Jan 2016; accepted 21 Jan 2016; published 3 Feb 2016

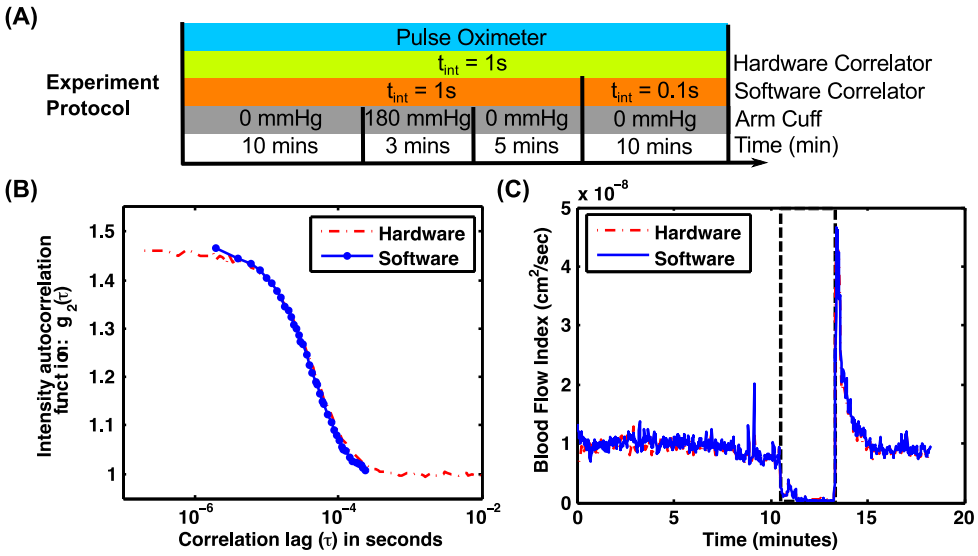

Fig. 3. Accurate estimates of blood flow with real-time software correlator. (A) Protocol for validating accuracy of blood flow measured with software correlator. For these validation experiments, the probe was placed on subject forearms, and an arm cuff was placed on the subject's bicep on the same side of the probe. (B) Representative intensity temporal auto-correlation functions estimated by the software correlator (40 delay times, solid blue line with solid blue markers) and a commercial hardware correlator (256 delay times, dashed red line) using an integration time of 1 s, under baseline conditions. (C) Dynamics of the tissue blood flow index, estimated by fitting the hardware (dashed red lines) and software (solid blue lines) correlator data to a diffusion model (Eq. (2), Appendix 1). Vertical dashed black lines bound the period of arm-cuff occlusion.

ison studies, the outputs of the detectors were split between a commercial hardware correlator (Correlator.com, Bridgewater, NJ) and our custom software correlators. Correlation functions derived from the same source-detector separation were averaged. All *in vivo* experiments were approved by the Institutional Review Board of the University of Pennsylvania, and a total of eight subjects were recruited for this study.

4.1. Software correlator provides accurate estimates of flow

We first demonstrate that the real-time software correlator accurately estimates blood flow in humans under baseline conditions and during an arm cuff ischemia (see Fig. 3(A)). For these validation experiments, a blood pressure cuff was placed around the subject's bicep (on the same arm as the probe). With the subject lying supine on a comfortable bed, an optical probe with embedded sources and detector fibers (2.5 cm separation) was secured on the subject's forearm. A commercial pulse oximeter (Rad-9, Masimo, Irvine, CA) monitored the subject's heart rate, and the heart rate data was recorded on the computer. The integration times (alternatively, the correlation function frame rate) of both hardware and software correlators were fixed at 1 s. After 10 minutes of baseline condition measurements, the blood flow in the arm was reduced for 3 minutes, by inflating the blood pressure cuff to 180 mmHg using a Tourniquet system (Zimmer Inc., Warsaw, IN). The experiment concluded with 5 minutes of post-occlusion data, and 10 minutes of baseline data with the software correlator set to record at a frame rate of 10 Hz (*i.e.*, increased from 1 Hz).

#255500 Received 14 Dec 2015; revised 20 Jan 2016; accepted 21 Jan 2016; published 3 Feb 2016

The accuracy of the software correlator for estimation of the intensity autocorrelation function is evident from representative intensity correlation curves in Fig. 3(B). The correlation function measured with the software correlator overlaps the 'gold-standard' hardware correlator values. Note, both correlators average over the 2 detector channels, with an average photon count rate of ~ 200 KHz. Also note, the correlation functions decay to a minimum value of 1 at delay times of ~ 200 μs, which is close to the maximum delay time used by the software correlator. Correlation measurements beyond these time scales are not useful. Thus, the software correlator estimates flow from the intensity correlation functions at the delay times most sensitive to blood flow changes. We refer the interested reader to Fig. 10 in Appendix 3 for comprehensive comparisons of blood flow measured with the hardware and software correlators from 8 subjects; differences in the blood flow indices measured by the two devices were not statistically significant ($p = 0.13$).

Figure 3(C) shows the blood flow dynamics estimated from hardware and software correlation data. The $\sim 100\%$ reduction in blood flow, due to cuff-ischemia, is clearly monitored by the software correlator. Tissue blood flow indices were estimated by fitting the intensity correlation functions to a semi-infinite geometry solution of the correlation diffusion equation (Eq. (2), Appendix 1). For this representative subject, the baseline tissue optical properties were measured to be $\mu_a = 0.16$ cm^{-1} and $\mu_s' = 4.28$ cm^{-1}, using a frequency domain diffuse optical spectroscopy instrument (Imagent, ISS Inc., IL, USA). These measurements also clearly demonstrate that 40 delay times between 1 μs and 125 μs are sufficient (more than sufficient) to accurately fit for a tissue blood flow index.

4.2. High speed measurements of baseline blood flow reveals pulsatile flow dynamics

We next demonstrate the ability of the real-time software correlator to measure high speed blood flow dynamics in human subjects under baseline conditions. Figure 4 displays the results of high-speed blood flow monitoring of baseline flow in the arm (*i.e.*, using the last 10 minutes of data from the previous experiment, Fig. 3(A)). Figure 4(A), shows representative intensity autocorrelation functions measured with a total integration time of 1 s. The solid red line is the correlation function measured by the hardware correlator (1 curve obtained at an integration time of 1 s). The solid blue circles, represent the correlation function values obtained at discrete delay times (*i.e.*, 40 delay times between 1 μs to ~ 250 μs) derived over the same time period with the high speed software correlator (data associated with 10 curves obtained at an integration time of 0.1 s each). In effect, the hardware correlator smears out the rapid fluctuations of the intensity correlation function. Figure 4(B) displays the blood flow index estimated using both the hardware (solid red line) and the high-speed software correlator (solid blue line), during the baseline period of 10 minutes; flow indices were determined by fitting the measured intensity autocorrelation functions to a semi-infinite geometry solution of the correlation diffusion equation (Eq. (2), Appendix 1).

At first glance, the blood flow index estimated using the high temporal resolution software correlator data appears to be very noisy. However, a more careful observation of the data, such as shown in the 15 s extracted time-window in Fig. 4(C), reveals significant temporal structure that corresponds to the pulsatile nature of tissue blood flow. The hemodynamics of the entire cardiac cycle is captured, including the 'dicrotic notch' which is the result of a brief increase in pressure (and thus flow) following closure of the aortic valve. The resolution of the dicrotic notch is particularly exciting, since it is rarely observed, *i.e.*, it is seen only when using high quality high speed instrumentation such as arterial line tracings. Further, as is evident from the solid red line, the blood flow index estimated using the hardware correlator averages out these fluctuations. The cardiac pulsatility is further confirmed by frequency spectrum of the data shown in Fig. 4(D). We refer the interested reader to Fig. 11 in Appendix 3 for comparisons of

#255500 Received 14 Dec 2015; revised 20 Jan 2016; accepted 21 Jan 2016; published 3 Feb 2016

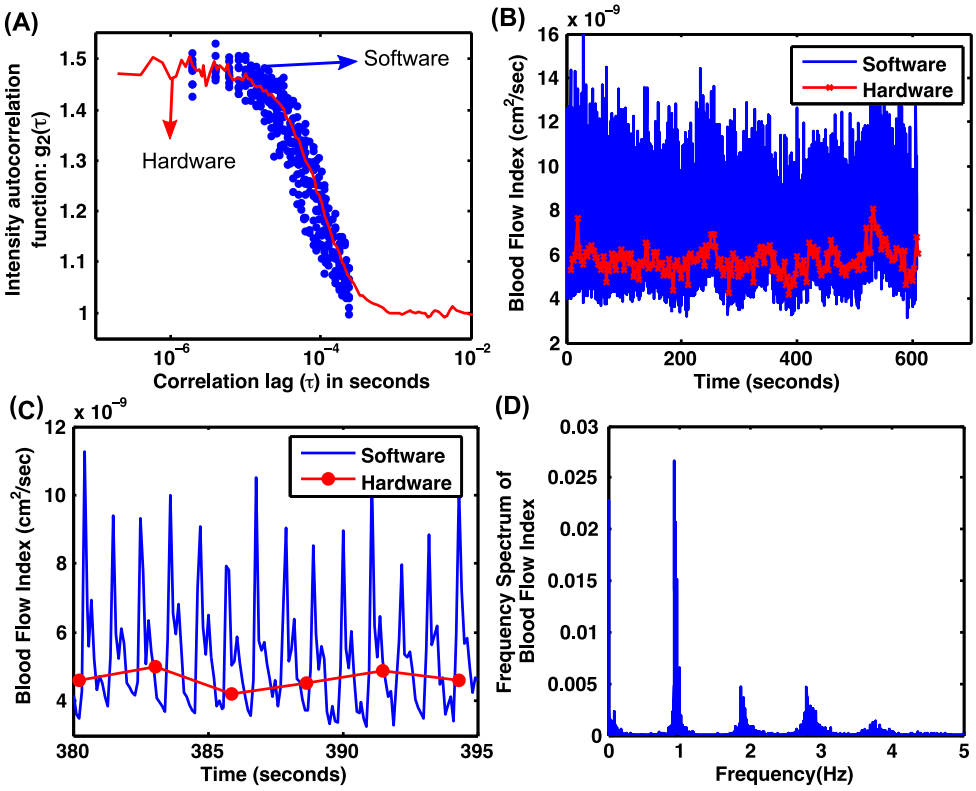

Fig. 4. Pulsatile blood flow measured with the real-time software correlator. (A) Data at discrete time points from 10 intensity temporal autocorrelation functions obtained with the software correlator (blue circles, 0.1 s integration time), and one intensity temporal autocorrelation function measured by the hardware correlator over the same duration (solid red line, 1 s integration time). (B) Natural fluctuations in the tissue blood flow index under baseline conditions as measured with the high speed software correlator (blue) and the lower speed hardware correlator (red). Blood flow indices were derived by fitting the measured intensity autocorrelation functions to a semi-infinite solution of the correlation diffusion equation (Eq. (2), Appendix 1) (C) ~ 15 s extract of baseline blood flow fluctuations, clearly demonstrating that the fluctuations in the blood flow index are a result of the pulsatile nature of blood flow. Notice, the entire cardiac cycle is clearly resolved, including the 'dicrotic notch', *i.e.*, the second flow peak of smaller magnitude within the cycle, corresponding to aortic valve closure. (D) The frequency spectrum of the baseline blood flow indices measured with the software correlator, highlighting the heart rate as ~ 0.9 Hz, with corresponding harmonics at 1.8, 2.7 and 3.6 Hz

the heart rates estimated with DCS, and a pulse oximeter from 8 healthy volunteers; statistically significant differences in the heart rate frequencies measured by the two devices were not found ($p = 0.76$).

The clear resolution of pulsatile flow dynamics, and the entire cardiac cycle, is the first significant physiological result of our paper. These fluctuations are often misconstrued as noise, and indeed, researchers have traditionally used integration times of 1 to ~ 2.5 seconds, in order to average out these fluctuations. Insufficient measurement speed, averages out useful information including beat-to-beat variations in blood flow. Moreover, measurements at intermediate

#255500 Received 14 Dec 2015; revised 20 Jan 2016; accepted 21 Jan 2016; published 3 Feb 2016

Table 1. Baseline fluctuations in tissue optical properties over 10 minutes measured on forearm and brain of 3 healthy volunteers

	Subject#	Absorption Coefficient $(\mu_a^0 \pm \Delta\mu_a)$ cm^{-1}	Scattering coefficient $(\mu_s'^0 \pm \Delta\mu_s')$ cm^{-1}
Forearm	1	0.415 ± 0.002	3.763 ± 0.068
	2	0.144 ± 0.002	4.928 ± 0.070
	3	0.184 ± 0.004	4.120 ± 0.090
Brain	1	0.125 ± 0.002	6.310 ± 0.090
	2	0.096 ± 0.001	7.232 ± 0.067
	3	0.128 ± 0.002	8.599 ± 0.148

sampling rates (*e.g.* $1-2$ Hz) do not fully resolve pulsatile dynamics and can lead to aliasing artifacts. For clarity, we have shown fluctuations in the correlation functions, sampled at 10 Hz in this characteristic example. In practice, our *in vivo* data is sampled at $20-50$ Hz; the measured photon count rates have an impact on the signal-to-noise of the measurements. We discuss these signal to noise considerations in a separate section.

4.3. Fluctuations in DCS blood flow index are primarily due to changes in blood flow

To elucidate the nature and origin of the fast blood flow index fluctuations more precisely, we carried out clarifying DOS and DCS experiments. In general, the DCS blood flow index depends parametrically on tissue blood flow and tissue absorption (μ_a) and scattering (μ_s') coefficients. As such, fluctuations in the tissue optical properties can also generate changes in the blood flow index. This relationship is quantitatively described by the DCS modified Beer-Lambert law [28] (see Appendix 2). Briefly, fluctuations in the intensity autocorrelation function define the variation of a 'DCS optical density' ($\Delta OD_{DCS}(\tau,\rho)$). The changes in the DCS optical density, in turn, are related to a linear combination of a change in blood flow (ΔF), a change in absorption coefficient ($\Delta\mu_a$), and a change in scattering coefficient ($\Delta\mu_s'$), via Eq. (3) in Appendix 2. Thus, by independently measuring the scattering and absorption coefficient changes, we can discern the fraction of the fluctuations in the DCS signal that are due to blood flow.

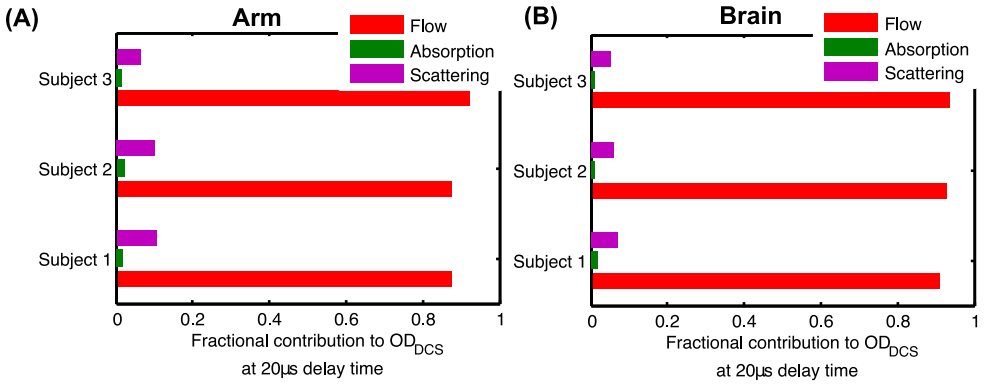

Fig. 5. Fractional contributions of flow, scattering and absorption to changes in the DCS signal measured from the arm (Panel A) and the brain (Panel B) of three healthy subjects.

#255500 Received 14 Dec 2015; revised 20 Jan 2016; accepted 21 Jan 2016; published 3 Feb 2016

Accordingly, the baseline fluctuations in tissue optical properties (μ_a and μ_s'), were monitored (at ~ 10 Hz) on the forearm and forehead of 3 volunteers, using a commercial frequency domain Diffuse Optical Spectroscopy instrument (Imagent, ISS Inc., IL), operating at 788 nm. Then, the high-speed software correlator was used to record the baseline fluctuations in the intensity autocorrelation functions from the same measurement spots.

The intensity correlation data gives the variation in DCS optical density. The average deviation from baseline of tissue optical properties were calculated from 10 minutes of DOS data. Table 1 summarizes these tissue absorption ($\mu_a^0 \pm \Delta\mu_a$), and scattering ($\mu_s'^0 \pm \Delta\mu_s'$) variations. The absorption and scattering contributions to the DCS optical density, respectively, are $d_a(\tau,\rho)\Delta\mu_a$ and $d_s(\tau,\rho)\Delta\mu_s'$; they are readily estimated (see Appendix 2 for details) using the measured fluctuations in optical properties (Table 1). Finally, the fractional absorption and scattering contributions to the DCS fluctuations were estimated from Eq. (3) in Appendix 2 as $\Delta OD_{DCS}(\tau,\rho)/d_a(\tau,\rho)\Delta\mu_a$, and $\Delta OD_{DCS}(\tau,\rho)/d_s(\tau,\rho)\Delta\mu_s'$ respectively. Figure 5 displays the results of these comparisons for the forearm and the brain. From this analysis, it is apparent that more than 90% of DCS fluctuations are driven by blood flow changes. This physiological finding, is the second important result of this paper. Pulsatile variation in the DCS signal reflect variations in blood flow.

4.4. Real-time software correlator can estimate cerebral autoregulation dynamics

We next explore the utility of the real-time software correlator in the context of a critical clinical application wherein rapid acquisition of blood flow information is needed: measurement of cerebral autoregulation dynamics [41]. Briefly, cerebral autoregulation (CVAR) refers to the mechanism by which normal (*i.e.* healthy) brain maintains relatively constant cerebral blood flow (CBF) despite fluctuations in mean arterial blood pressure (MAP) [55]. Importantly, CVAR is often impaired after brain injury; in this scenario, CBF can vary in response to MAP variation [56, 57]. Moreover, the degree of CVAR impairment correlates with the initial severity of brain injury and is an independent predictor of outcome [41, 56, 58].

CVAR is typically measured using static or dynamic techniques [40] that rely on the detection of cerebral blood flow velocity, *e.g.*, derived by trans-cranial Doppler ultrasound. Here, we showcase the potential for monitoring dynamic autoregulation with DCS using the high speed real-time software correlator. We employ a standard approach for measuring CVAR dynamics. In particular, we measure the time-dependent changes in CBF resulting from transient increases in cardiac output, *i.e.*, following deflation of blood pressure cuffs applied to the thigh [41].

Figure 6(A) details the protocol used to measure dynamic cerebral autoregulation [41] from one healthy volunteer. With the subject lying supine, the optical probe was placed on the subject's forehead, over the frontal cortex. Two blood pressure (BP) cuffs were wrapped around the subject's thighs, about 10 cm above the knee. The subject's blood pressure was continuously monitored using a non-invasive finger pressure monitor (Finometer Pro, Finapress Medical Systems, Netherlands), and cerebral blood flow was measured with the real-time software correlator at a data acquisition rate of 20 Hz. After a 5 minute baseline measurement, the thigh cuffs were both inflated and held at 30 to ~ 40 mmHg above the subject's baseline systolic blood pressure (here 170 mmHg) for a period of 4 minutes. At the end of the inflation period, both cuffs were rapidly deflated by disconnecting the pressure pump. Two blood pressure manipulation trials were carried out, *i.e.*, the thigh cuffs were inflated and deflated twice. The experiment concluded with 4 minutes of baseline measurements. Typically, cerebral hemodynamics (*i.e.*, CBF and BP) from multiple thigh cuff 'trials' on the same subject are averaged. Here, we showcase the speed and measurement fidelity of the real-time software correlator, by estimating cerebral autoregulation dynamics using measurements from a *single* trial.

Cerebral blood flow (CBF) and blood pressure (BP) were continuously monitored through-

#255500 Received 14 Dec 2015; revised 20 Jan 2016; accepted 21 Jan 2016; published 3 Feb 2016

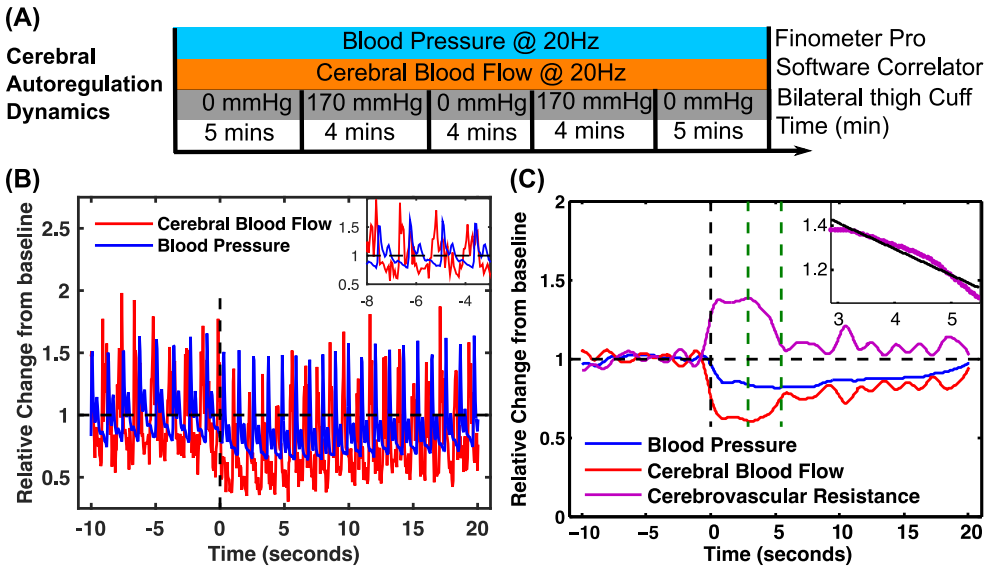

Fig. 6. Dynamic cerebral autoregulation estimated using the high-speed software correlator. (A) Protocol for monitoring cerebral autoregulation dynamics with the real-time software correlator. Here, the probe is placed on the subject's forehead over the frontal cortex. Two blood pressure cuffs were placed on the subject's thighs, about 10 cms above the knees. (B) Unfiltered measurements of relative cerebral blood flow (solid red lines) and blood pressure (solid blue lines) from a single bilateral thigh cuff deflation. Vertical dashed black lines indicate the time of cuff deflation. All measurements were normalized to a 10 s pre-deflation baseline. (Inset) $\sim$ 5s extract of the baseline period shows a phase difference between CBF and blood pressure. (C) Filtered relative cerebral blood flow (solid red lines) and blood pressure (solid blue lines) changes due to a bilateral cuff-deflation (dashed vertical black line at $t = 0$ s). The change in relative cerebrovascular resistance is also shown (solid magenta line). The two dashed vertical green lines denote the period of recovery of cerebrovascular resistance; a linear fit to this data is shown in the inset.

out the experiment at a data acquisition rate of 20 Hz. The relative *unfiltered* change in CBF ($rCBF = CBF(t)/CBF_0$) and BP ($rBP = BP(t)/BP_0$) from a *single trial* of blood pressure manipulation is displayed in Fig. 6(B). Here, time $t = 0$ (vertical dashed line) denotes the start of bilateral cuff deflation, and the solid red and blue lines denote the pulsatile dynamics of CBF and blood pressure, respectively. Both CBF and BP are normalized to their values during the 10 s pre-deflation baseline period. The sudden cuff deflation, causes a rapid increase in venous return and cardiac output; these effects produce a transient decrease in BP and CBF. This $\sim 20\%$ and $\sim 40\%$ decrease in average BP and CBF is clearly evident, even in the unfiltered measurements. Note that the high temporal resolution of the software correlation technique reveals a phase difference between CBF and blood pressure (see inset in Fig. 6(B)). Ultimately, it may be possible to use the *dynamics* of this phase shift as a biomarker of cerebral autoregulation [59–61]. We note however, that differences in pulse transit times to cerebral/peripheral vasculature may lead to 'offsets' in the phase-shift between the CBF and BP. Pulse transit times can potentially be measured by simultaneous blood flow and blood pressure recordings in the brain and arm. A more complete investigation of these issues is planned; for example, correction/calibration factors may need to be developed before the absolute value of the phase-shift can be utilized as a biomarker for cerebral autoregulation.

#255500 Received 14 Dec 2015; revised 20 Jan 2016; accepted 21 Jan 2016; published 3 Feb 2016

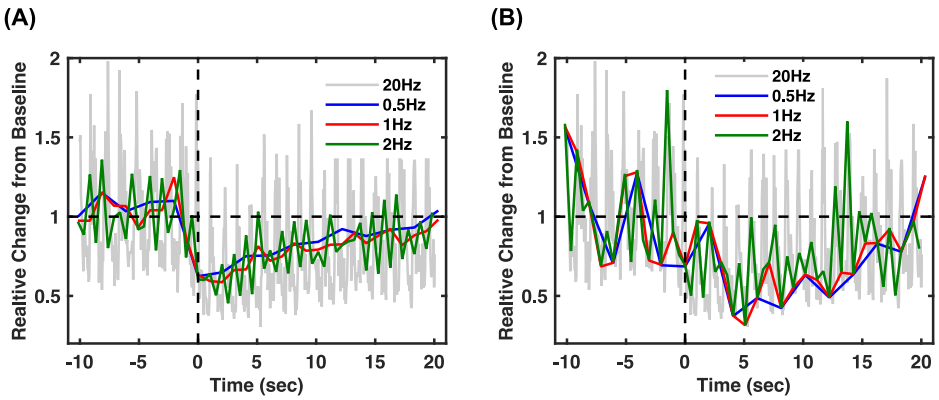

Fig. 7. Comparison of measurement of cerebral autoregulation dynamics at different CBF measurement rates. (A) Reduced data rates were achieved by averaging/integrating high-frequency software correlator intensity temporal autocorrelation functions (20 Hz, gray) to 0.5 Hz (blue, a common hardware correlator data rate), 1 Hz (red) and 2 Hz (green). Measurements at 0.5 and 1 Hz are highly averaged and capture the $\sim 20\%$ baseline fluctuation in CBF. The 1 Hz data rate identifies, but only poorly resolves the heart rate fluctuations. None of lower frequency data can accurately capture the instantaneous decrease in CBF due to cuff deflation. Note that this form of averaging is an accurate representation of data integration in the hardware correlators. (B) Reduced data rates achieved by down-sampling the high-frequency software correlator intensity autocorrelation functions. Down-sampled CBF data is quite noisy.

In order to quantify dynamic cerebral autoregulation, the measured CBF and BP dynamics were first filtered to remove heart rate effects using a low pass filter with a cutoff frequency set to 75% of the heart rate. The filtered autoregulation measurements from a single trial are displayed in Fig. 6(C), *i.e., rCBF* by solid red line and *rBP* by solid blue lines, respectively. Importantly, Fig. 6(C) also shows the change in cerebrovascular resistance (solid magenta line): $rCVR = rBP/rCBF$. The vertical dashed black line indicates the start of cuff deflation.

In combination, the changes in CBF, BP and CVR, describe the autoregulation process. The sudden decrease in BP and CBF is characterized by an almost instantaneous increase in vascular resistance, followed by a gradual return to baseline due to the autoregulation process. The rate of change of *rCVR*, $\mathrm{d}rCVR/\mathrm{d}t$, can be estimated from the linear decrease in *rCVR* between the two vertical dashed green lines (see inset in Fig 6(B)). Finally, a rate of regulation can be calculated, $ROR = (\mathrm{d}rCVR/\mathrm{d}t)/\Delta BP$, wherein ΔBP is the maximum decrease in *rBP* from baseline. For this representative subject, the rate of regulation is 0.66 sec; *i.e.*, a 66% change in resistance is required per second in order to autoregulate a 1% change in blood pressure. We emphasize that this entire analysis was carried out from a *single trial* without averaging.

The utility of the real-time software correlator for measurements of cerebral autoregulation dynamics is evident from comparisons with lower speed CBF measurements of traditional hardware correlators. We first averaged (Fig. 7(A)) the intensity correlation functions acquired at 20 Hz (gray lines) to CBF measurements at 0.5 Hz (blue lines), 1 Hz (red lines) and 2 Hz (green lines). For example, for every CBF measurement at 1 Hz, 20 intensity autocorrelation functions originally measured at 20 Hz were binned and averaged. This manner of averaging simulates increased integration time in hardware correlators. A second approach, down-samples (Fig. 7(B)) the 20 Hz data to a lower data rate.

Once averaged (or down-sampled), a blood flow index was estimated by fitting the averaged (or down-sampled) intensity autocorrelation function with the solution to the correlation diffu-

#255500 Received 14 Dec 2015; revised 20 Jan 2016; accepted 21 Jan 2016; published 3 Feb 2016

sion equation (Eq. (2), Appendix 1). Figure 7(A) shows the effects of averaging on measurement of cerebral autoregulation dynamics from a single trial. Unsurprisingly, the integrated CBF measurements at 0.5 Hz and 1 Hz completely average the pulsatile blood flow fluctuations. At 2 Hz, the pulsatile flow is identified, but is aliased and is therefore poorly resolved. When compared to the filtered autoregulation curves in Fig. 6(C), these averaged measurements exhibit greater baseline noise, appear to exhibit timing inaccuracies with respect to cuff deflation (*i.e.* vertical dashed line), and do not show an instantaneous decrease in CBF due to cuff deflation. These detrimental effects are clearly evident in the down-sampled data (Fig. 7(B)) wherein the fluctuations/noise in CBF measurements are sometimes indistinguishable from CBF changes due to the thigh cuff deflation. In both cases, additional filtering (or averaging) can reduce the noise, but such averaging/filtering also temporally broadens the autoregulation 'signal', in large part due to reduced temporal resolution. Note, an experiment with the hardware correlator will be affected by averaging and (to a lesser extent) down-sampling, due to data transfer lags and software overheads.

The best quality data is obtained by measuring CBF dynamics at the highest data rates possible, *i.e.*, with the real-time software correlator. This observation highlights the value of the real-time correlator for continuous monitoring of autoregulation. The demonstration of instrumentation to monitor cerebral autoregulation dynamics in this manner is arguably the most important result of this paper.

4.5. Signal-to-noise ratio considerations for fast blood flow measurements with DCS

We conclude this paper with a discussion about signal-to-noise ratio (SNR) considerations for fast flow measurements with DCS. The ability of the real-time software correlator to detect high frequency flow dynamics (Fig. 4(A)) has been demonstrated. Ultimately however, the ability to discern meaningful flow information, *i.e.*, blood flow index variation, will depend on the *fidelity* of measured autocorrelation functions, which, in turn, depends on the number of detected photons, *i.e.*, the detected light intensity, and the amount of averaging *i.e.*, measurement integration time. The precise dependence of the measurement SNR on light intensity and integration time can be ascertained using a photon correlation noise model adapted for diffuse light (*i.e.*, DCS noise model) [62].

To confirm the accuracy of the DCS noise model at the short integration times permitted by our new software correlator, we systematically characterized correlation noise in a liquid tissue phantom. The liquid tissue phantom consisted of 21.7 ml/l of 30% Intralipid (Fresenius Kabi, Uppsala, Sweden) with 1.88 ml/l of India ink (Higgins, Black India 44201, MA) resulting in optical properties of $\mu_a = 0.16\ \mathrm{cm}^{-1}$ and $\mu_s' = 4.32\ \mathrm{cm}^{-1}$. An optical probe with 1.5 cm source-detector separation was placed on the liquid surface to simulate a semi-infinite geometry. The integration time was systematically varied as depicted in Fig. 8(A). Further, the photon count rate was also systematically varied using an attenuator on the source arm.

Following the conventions of a previous DCS noise model [62], we define 'noise' to be the standard deviation of the measured intensity autocorrelation function, $\sigma(\tau)$ (*i.e.*, $\sigma(\tau)$ is the standard deviation of $g_2(\tau)$ measured over the duration of the experiment). We then define the SNR to be $\zeta(\tau) = (g_2(\tau) - 1)/\sigma(\tau)$. Here, we make the inherent assumption that fluctuations in the measured autocorrelation function are due to random noise (appropriate for these tissue phantom experiments). Figure 8 displays the result of the SNR characterization from the liquid phantom. In panels (B) and (D), we have plotted the measurement noise as a function of the integration time of the software correlator at delay times of 20 μs and 80 μs respectively, for three different photon detection signal levels - 20 kHz (blue circles), 50 kHz (red squares), and 94 kHz (black diamonds). In each case, the measurements are fit to a DCS noise model [62]. In a similar vein, panels (C) and (E) show the corresponding measurements of signal-to-noise ratio.

#255500 Received 14 Dec 2015; revised 20 Jan 2016; accepted 21 Jan 2016; published 3 Feb 2016

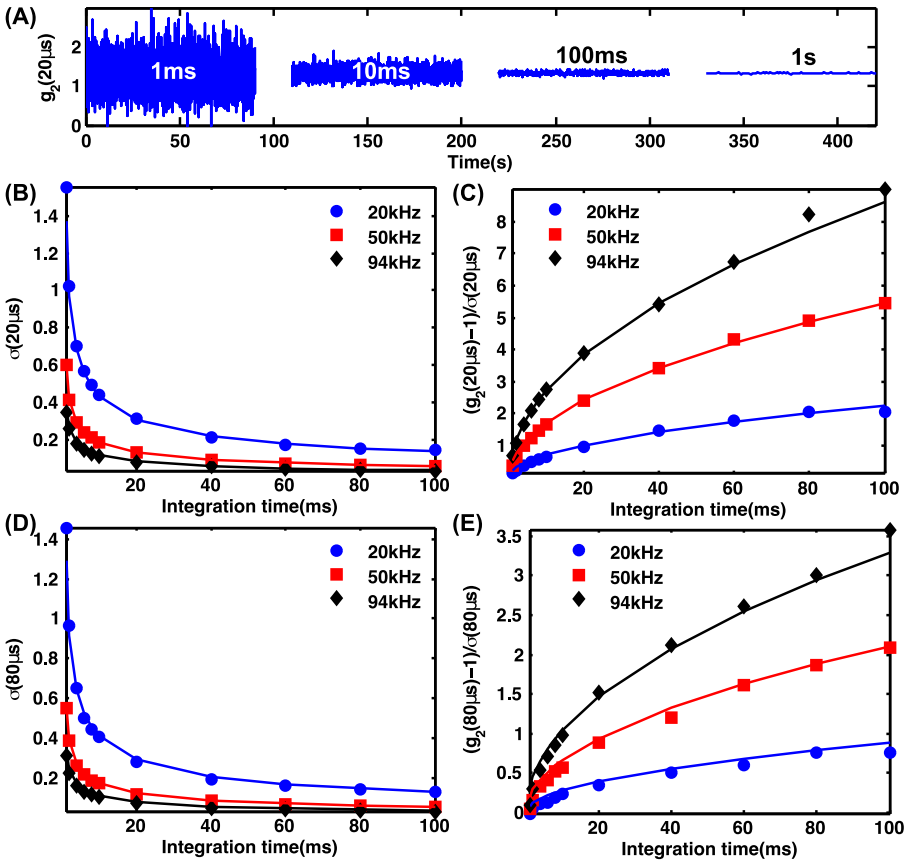

Fig. 8. Estimation of signal-to-noise ratios due to data from a liquid phantom. (A) Sample intensity autocorrelation values measured at a delay time of 20 μs for different integration times. Lower integration times are more noisy, since averaging is reduced. Panels (B) and (D) plot the standard deviation of measured intensity autocorrelation functions versus integration time and photon count rates, at delay times of 20 μs and 80 μs respectively. Panels (C) and (E) plot the corresponding signal-to-noise ratios. All measurements are fit to a DCS correlation noise model [62](solid lines).

For each condition examined in Fig. 8, the measured noise (dots) agrees well with the DCS noise model (solid lines). Thus, we confirm that the DCS noise model provides a theoretical framework that would allow an experimenter to pick the right photon count rates, integration times, and delay times to achieve a desired SNR.

Figures 8(B) and (D) clearly show that the measurement noise decreases with increased averaging (increased integration times) and improved signal (increased detected photon count rates). Correspondingly, as is evident from Figs. 8(C) and (E), the signal-to-noise ratio increases with integration time and photon count rates. From these measurements, one can observe that a SNR of 1 at acquisition rates of 25 Hz (40 ms integration time), requires a photon count rate of $\sim$ 20 kHz. More realistic signal levels of $\sim$ 50 kHz will permit acquisition rates of $\sim$ 50 Hz at SNR of 1.

More practically, this experiment and analysis enables us to estimate optimum operating parameters for fast *in vivo* measurements of blood flow. For *in vivo* experiments, we are interested in the ability of the correlator to resolve dynamics at particular frequencies. An obvious fre-

#255500 Received 14 Dec 2015; revised 20 Jan 2016; accepted 21 Jan 2016; published 3 Feb 2016

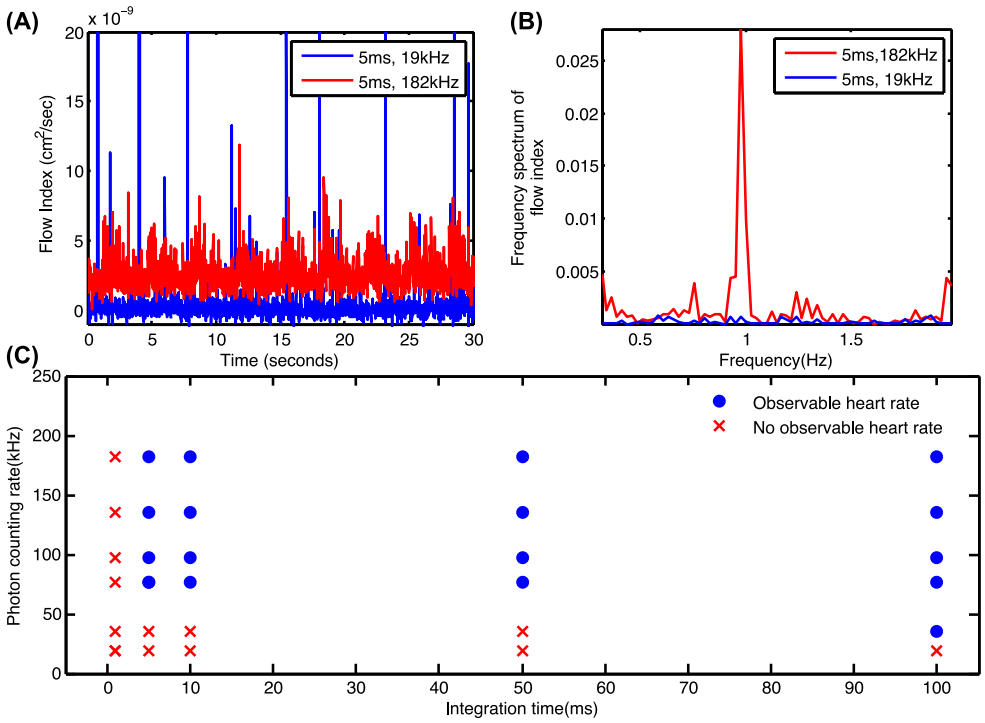

Fig. 9. Optimization of experimental parameters to isolate heart rate with fast blood flow measurements. (A) Natural fluctuations in blood flow index acquired on the arm are plotted as a function of time for 19 kHz (solid blue lines) and 182 kHz (solid red lines) photon count rates and 5 ms integration times. (B) Corresponding frequency spectra of blood flow index dynamics show a clear peak at the heart rate frequency for the higher photon count rate data. (C) Scatter plot showing which photon count rates and integration times permit the identification of the heart rate in *in vivo* data. Red crosses indicate parameters where heart rate could not be identified, while solid blue circles indicate parameters where heart rate was successfully identified.

quency of interest is that of the heart rate, especially because physiological perturbations in flow are oftentimes slower than the heart rate. With a setup similar to Fig. 2, we measured baseline blood flow dynamics, at integration times ranging from 1 ms to 100 ms, with photon count rates manipulated via laser attenuation. Data was collected for a total of $30 \sim 40$ s at each setting.

Figure 9(A) shows the representative fluctuations in blood flow index over a period of 30 seconds measured with a 5 ms integration time, at photon count rates of 19 kHz in blue and 182 kHz in red. Figure 9(B) shows the corresponding frequency spectra; a clear peak at ~ 1 Hz is visible in the measurements at 182 kHz indicating that the heart rate is well resolved at the high photon count rate, but not at the smaller signal levels. Figure 9(C) shows the result of the experiment wherein multiple integration times and photon count rates were tested on similar data. The solid blue circles indicate the measurement parameters where the heart rate was clearly resolved, *i.e.*, the maximum frequency component in the spectrum was between 0.8 Hz and 1.2 Hz. Red crosses, indicate parameters were the heart rate was not resolved. From these measurements, we conclude that photon count rates of $\sim 50 - 100$ kHz are ideal for fast flow measurements over a large range of acquisition rates. Importantly, this experiment provides a

#255500 Received 14 Dec 2015; revised 20 Jan 2016; accepted 21 Jan 2016; published 3 Feb 2016

practical framework to select an appropriate data acquisition rate for accurate estimation of blood flow.

5. Discussion

Traditionally, blood flow has been measured with DCS at relatively slow data rates ($0.5-1$ Hz). Therefore fluctuations due, for example, to heart beats have often been considered as noise that should be averaged in the measured autocorrelation function (for example, Fig. 4(A)); this noise assignment, in turn, prompted the need for increased temporal averaging. Interestingly, although heartbeat oscillations are well recognized in the NIRS community [63–65], the DCS community has been comparatively slow to appreciate the full potential of fast blood flow measurements.

The primary goal of the present contribution is to report development and testing of new, optimized instrumentation and software that fulfills an unmet clinical need for continuous fast measurements of blood flow with DCS. Aside from validating the accuracy of the software correlator, the work provides a rigorous overview of timing and sampling considerations. Further, for the first time, we have characterized the signal-to-noise characteristics of DCS at low integration times, and in the process we have validated the prevailing DCS noise models for fast measurements of blood flow. Critically, these characterization experiments provide a framework for the identification of optimum data acquisition parameters.

We demonstrated sustained/continuous blood flow measurements at speeds up to 100 Hz *in vivo* at typical source detector separations of 2.5 cm. Measurement speeds are limited only by the available photon count rates. To our knowledge, the results represent the fastest reported blood flow measurements achieved with DCS, using either hardware or software correlators. We have leveraged this high temporal resolution data to learn about new flow physiology, and to highlight new opportunities for monitoring of cerebral health.

1. We showed that *blood flow* accounts for over 90% of the pulsatile DCS signal, thereby identifying the origin of the fluctuations in the pulsatile DCS signal *in vivo*. This discovery was facilitated by the improved speed afforded by the software correlator.

2. Our work shows that cerebral autoregulation dynamics can be studied using DCS. The high data rates afforded by the software correlator were critical for this application (see for example Fig. 7). This demonstration is important because cerebral autoregulation holds tremendous potential as a biomarker of brain injury, and the use of DCS for this application will permit non-invasive and real-time monitoring of brain injury.

3. Our measurements of blood flow pulsatility clearly resolve features of the entire cardiac cycle including the dicrotic notch, demonstrating data quality akin to high speed arterial line tracings. Such high temporal resolution holds potential for measurements of compliance in cerebrovascular circulation; for example, flow pulsatility measured on arm and the brain could reveal differences in arterial elasticity. Measurements of cerebrovascular compliance can potentially identify arterial stiffening or dissection, *i.e.*, information indicative of diseases such as atherosclerosis, amyloidosis and stroke.

The software correlator we have demonstrated is relatively easy to implement on a standard personal computer. When compared to the fastest DCS hardware correlators [50], our measurements are faster, can be sustained for longer durations, and do not require averaging over many detectors. With the new software correlator design, we adopt a slightly different approach compared to previous studies, *i.e.*, we use direct computation of the autocorrelation with the shift-and-add method [44], instead of highly efficient fast Fourier transforms (FFT) [52,53].

#255500 Received 14 Dec 2015; revised 20 Jan 2016; accepted 21 Jan 2016; published 3 Feb 2016

In general, the FFT approach can be fast for large data sets, *i.e.*, when the autocorrelation function needs to be computed at hundreds of delay times. By limiting the autocorrelation function computation to 40 delay times, however, our software correlator easily removes this inefficiency, is arguably faster, and is less memory intensive than the FFT approach. Moreover, we can readily adapt our correlator for a single delay time operation (which would remove all speed advantages offered by the FFT method) and use the DCS modified Beer-Lambert law [28] to estimate blood flow dynamics.

6. Conclusions

We have reported the development of a new real-time software correlator for fast measurements of blood flow with Diffuse Correlation Spectroscopy. We validated the new device against gold-standard commercial hardware correlators, and we established timing/sampling and intensity guidelines for measurements with sufficient signal-to-noise ratios. We also highlighted the potential value for the new device by using it to separate pulsatile blood flow contributions to the fluctuating DCS signal and to monitor cerebral autoregulation dynamics *in vivo*.

Appendix 1: solution to correlation diffusion equation

Formally, the transport of the *electric field* autocorrelation function ($\mathbf{E}(t)$), $G_1(\tau) \equiv \langle \mathbf{E}^*(t) \cdot \mathbf{E}(t+\tau) \rangle$, is modeled by the Correlation Diffusion Equation (CDE) [2, 8]. The normalized *electric field* autocorrelation function ($g_1(\tau) = G_1(\tau)/G_1(0)$) is related to the measured (normalized) *intensity* autocorrelation function ($g_2(\tau)$) via the Seigert relation [66]; $g_2(\tau) = 1 + \beta |g_1(\tau)|^2$, and a tissue blood flow index (proportional to blood flow) can be estimated by fitting $g_1(\tau)$ to a geometry dependent solution of the Correlation Diffusion Equation. In the clinically relevant semi-infinite geometry, with illumination and detection at a single point separated by a distance ρ (e.g., Fig. 1), the solution to the CDE is given by [2, 8]

$$g_1(\tau,\rho) = \frac{r_b \exp(-\kappa_D(\tau) r_1) - r_1 \exp(-\kappa_D(\tau) r_b)}{r_b \exp(-\kappa_D(0) r_1) - r_1 \exp(-\kappa_D(0) r_b)} \tag{2}$$

Here, $\kappa_D(\tau)^2 = [3\mu_a(\mu_a + \mu_s')(1 + 2\mu_s'^2 k_0^2 F\tau/\mu_a)]$ and F is the blood flow index to be estimated. $r_1^2 = (l_{tr}^2 + \rho^2)$, $r_b^2 = ((2z_b + l_{tr})^2 + \rho^2)$, $l_{tr} = 1/(\mu_a + \mu_s')$ and $z_b = 2l_{tr}(1 + R_{eff})/(3(1 - R_{eff}))$ are constants dependent on the tissue absorption (μ_a) and scattering (μ_s') coefficients. R_{eff} is the effective reflection coefficient accounting for the refractive index mismatch between the tissue (n) and the medium (n_{out}), and $k_0 = 2\pi n/\lambda$, is the magnitude of the light wave vector in the medium.

Appendix 2: DCS modified Beer-Lambert law

We recently introduced a DCS modified Beer-Lambert law [28], that allows rapid computation of *changes* in blood flow by solving a system of linear equations. In this approach a 'DCS Optical density' is computed in the baseline ($OD_{DCS}^0(\tau,\rho) \equiv -\log(g_2^0(\tau,\rho) - 1)$) and perturbed ($OD_{DCS}(\tau,\rho) \equiv -\log(g_2(\tau,\rho) - 1)$) states, and the change in blood flow is determined from the change in DCS optical density ($\Delta OD_{DCS}(\tau,\rho) = OD_{DCS}(\tau,\rho) - OD_{DCS}^0(\tau,\rho)$) and the DCS Modified Beer-Lambert law for flow:

$$\Delta OD_{DCS}(\tau,\rho) = -\log\left(\frac{g_2(\tau,\rho) - 1}{g_2^0(\tau,\rho) - 1}\right) \approx d_F(\tau,\rho)\Delta F + d_a(\tau,\rho)\Delta\mu_a + d_s(\tau,\rho)\Delta\mu_s'. \tag{3}$$

Here, ΔF, $\Delta\mu_a$ and $\Delta\mu_s'$ are the changes in flow, absorption and scattering from their baseline values of F^0, μ_a^0 and $\mu_s'^0$ respectively. The multiplicative weighting factors $d_F(\tau,\rho)$, $d_a(\tau,\rho)$,

#255500 Received 14 Dec 2015; revised 20 Jan 2016; accepted 21 Jan 2016; published 3 Feb 2016

and $d_s(\tau,\rho)$ are evaluated by computing the appropriate derivative of the DCS optical density for the baseline state, i.e., $d_F(\tau,\rho) \equiv \partial OD^0_{DCS}/\partial F$, $d_a(\tau,\rho) \equiv \partial OD^0_{DCS}/\partial \mu_a$, and $d_s(\tau,\rho) \equiv \partial OD^0_{DCS}/\partial \mu_s'$ [28].

Notice that the relative contributions of blood flow, tissue absorption, and tissue scattering changes to the total DCS signal change can easily be determined with the DCS modified Beer-Lambert framework (e.g., blood flow changes are responsible for $(d_F \Delta F/\Delta OD_{DCS}) \times 100$ percent of the signal change).

Appendix 3: Validation of blood flow indices and heart rates estimated with software correlator

We found excellent agreement between the baseline blood flow indices measured with the hardware and software correlators in 8 subjects (Fig. 10). Figure 10(A) shows the result of a linear regression analysis between the blood flow indices measured using the software correlator (BFI_s, x-axis) and the hardware correlator (BFI_h, y-axis). The regression line (solid red line) with slope of 0.967 and an excellent goodness of fit ($R^2 = 0.9729$) clearly demonstrates that both instruments measure the same blood flow. Further, a Bland-Altman plot of the difference between the two blood flow indices versus their mean reveals no significant difference between the two techniques ($p = 0.13$, see Fig. 10(B)). Therefore, the software correlator technique does accurately measure the tissue blood flow index.

Our hypothesis that temporal fluctuations in the DCS autocorrelation functions are the result of arterial pulsation was validated by comparing the frequency of these temporal fluctuations against the heart rate measured with a commercial pulse oximeter (Fig. 11). For each subject, the frequency spectrum of the blood flow index dynamics was computed; the first peak in the spectrum was used to estimate the subject's baseline/average heart rate (see for example Fig. 4(C)). Figure 11(A) displays the result of linear regression analysis on the heart rate estimated using the software correlator (x-axis) versus the 'gold-standard' heart rate measurement from a commercial pulse oximeter; a regression slope of 1 and a goodness of fit of 0.998

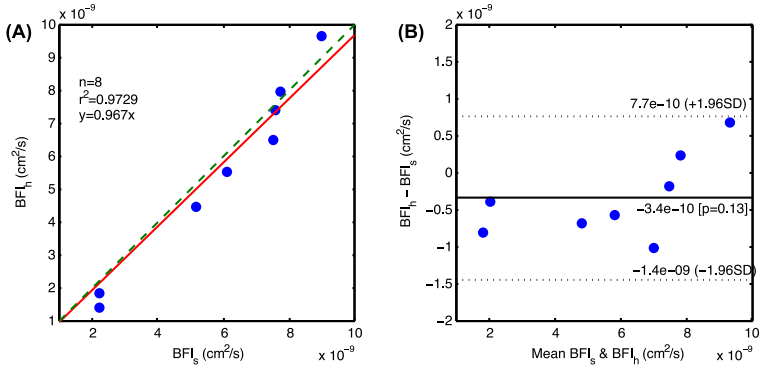

Fig. 10. Comparisons of blood flow indices measured using software and hardware correlators under baseline conditions from 8 subjects. (A) Scatter plot of blood flow indices estimated using the software correlator (BFI_s, x-axis) and hardware correlator (BFI_h, y-axis). Solid blue circles represent each measurement, the dashed green line is a 1 : 1 line, and the solid red line is a line of linear regression line. The slope of the regression line is 0.967 denoting good agreement between the two techniques. (B) Bland-Altman plot that represents the average (x-axis) and difference (y-axis) of the estimated blood flow indices. All measurements are within the 95% confidence lines (dashed horizontal black lines) indicating good agreement between the techniques.

#255500 Received 14 Dec 2015; revised 20 Jan 2016; accepted 21 Jan 2016; published 3 Feb 2016

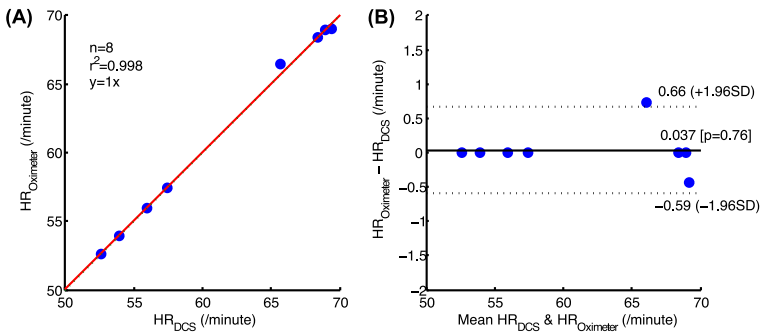

Fig. 11. Comparison of heart rates estimated using the software correlator (e.g. from frequency spectrum in Fig. 4(C)) and a commercial pulse oximeter, under baseline conditions from 8 subjects. (A) Scatter plot of heart rate estimate estimated using the software correlator (HR_{DCS}, x-axis) and commercial pulse oximeter ($HR_{Oximeter}$, y-axis). Solid blue circles represent each measurement, the dashed green line is a 1 : 1 line, and the solid red line is a line of linear regression line. The slope of the regression line is 1 denoting excellent agreement between the two techniques. (B) Bland-Altman plot that represents the average (x-axis) and difference (y-axis) of the estimated heart rates. All measurements are within the 95% confidence lines (dashed horizontal black lines) indicating good agreement between the techniques.

show excellent agreement between the two measurements. This agreement is confirmed in a Bland-Altman analysis, Fig. 11(B), which clearly shows no significant difference between the two techniques ($p = 0.76$).

Acknowledgments

We are grateful to Dr. Daniel Licht, Kenneth Abramson and Dr. David Busch for their valuable discussion and assistance in the measurements. We acknowledge support from the National Institutes of Health (R01 – NS060653, 8P41 – EB015893), the Application Foundation and Advanced Technology Research Program of Tianjin (14CZDJC33100) and the China Scholarship Council (201306250114). ABP acknowledges support from the American Heart Association (14POST20460161).